Magnetomotive optical coherence elastography for relating lung structure and function in Cystic Fibrosis

Raghav K. Chhetri,[1] Jerome Carpenter,[2] Richard Superfine,[1] Scott H. Randell,[3] Amy L. Oldenburg[1,4]

[1]Department of Physics and Astronomy, University of North Carolina at Chapel Hill
[2]Curriculum in Applied Sciences and Engineering, University of North Carolina at Chapel Hill
[3]Cystic Fibrosis/Pulmonary Research and Treatment Center, University of North Carolina at Chapel Hill
[4]Biomedical Research Imaging Center, University of North Carolina at Chapel Hill

ABSTRACT

Cystic fibrosis (CF) is a genetic defect in the cystic fibrosis transmembrane conductance regulator protein and is the most common life-limiting genetic condition affecting the Caucasian population. It is an autosomal recessive, monogenic inherited disorder characterized by failure of airway host defense against bacterial infection, which results in bronchiectasis, the breakdown of airway wall extracellular matrix (ECM). In this study, we show that the *in vitro* models consisting of human tracheo-bronchial-epithelial (hBE) cells grown on porous supports with embedded magnetic nanoparticles (MNPs) at an air-liquid interface are suitable for long term, non-invasive assessment of ECM remodeling using magnetomotive optical coherence elastography (MMOCE). The morphology of *ex vivo* CF and normal lung tissues using OCT and correlative study with histology is also examined. We also demonstrate a quantitative measure of normal and CF airway elasticity using MMOCE. The improved understanding of pathologic changes in CF lung structure and function and the novel method of longitudinal *in vitro* ECM assessment demonstrated in this study may lead to new *in vivo* imaging and elastography methods to monitor disease progression and treatment in cystic fibrosis.

1. INTRODUCTION

Cystic Fibrosis (CF) is an autosomal recessive, monogenic inherited disorder characterized by failure of airway host defense against bacterial infection. The genetic defect in the cystic fibrosis transmembrane conductance regulator protein results in unusually thick, sticky mucus that adheres to the airway wall and leads to life-threatening lung infections. CF is the most common life-limiting genetic condition affecting the Caucasian population and there are ~30,000 CF patients in the United States alone. The median survival of CF patients is ~37 years.[1] In normal airways, a physiologically-regulated system results in adequate mucosal surface hydration, enabling coordinated, directional cilia beating that results in effective mucus transport. However, in CF lungs, the airway surface layer becomes relatively dehydrated and depleted preventing effective cilia beat. Impaired muco-ciliary clearance and hyper-viscous mucus that is not easily cleared by coughing creates a favorable environment for bacterial growth.[2] Chronic bacterial lung infection and recurring pulmonary exacerbations in CF patients ultimately result in declining lung function, respiratory failure and death. The infecting bacteria and the host inflammatory response produce extracellular degradative enzymes that cause bronchiectasis, *i.e.,* anatomic and histological changes to the bronchial airway including thickening, herniation, dilation, and increased tortuousness.[3] The breakdown of extracellular matrix (ECM) in bronchiectasis changes airway wall stiffness contributing to airway collapse and airflow obstruction, especially during exhalation.

Optical coherence tomography (OCT) and its recent extensions in elastography make it well suited to provide a platform for understanding mechanisms resulting in bronchiectasis in CF patients. OCT is an interferometric technique that performs noninvasive, high resolution, cross-sectional imaging of biological tissues by measuring the echoes of backscattered light.[4] OCT is an emerging technology in medicine as it enables real time, *in situ* visualization of tissue microstructures without the need to remove and process specimens.[5] Optical coherence elastography (OCE) is a recent extension to OCT in which internal microscopic deformations of tissues are imaged in response to applied mechanical stress.[6] Aside from OCE, various other elastography techniques such as ultrasound elastography[7] and magnetic
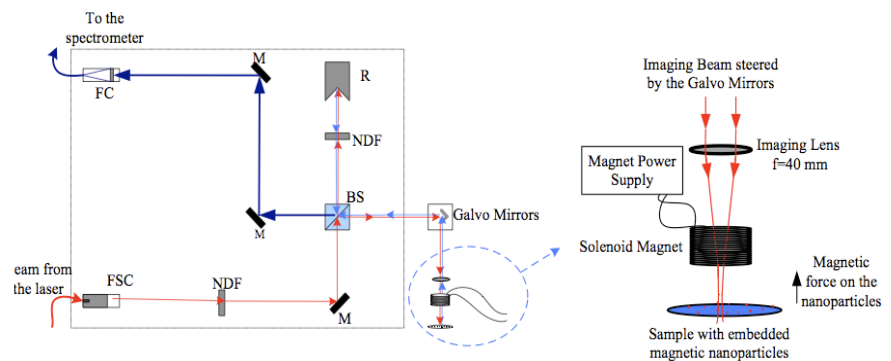
resonance elastography[8] are also used to image the biomechanical properties of soft tissues. Magnetic resonance imaging however is costly and time consuming whereas the imaging resolution in ultrasound is only between 100 to 200 μm. [9] OCE provides an inexpensive, real-time alternative to performing elastography in biological tissues with higher resolution than that achieved using ultrasound elastography.[10] OCE has previously been used to study arterial wall biomechanics by tracking endogenous arterial wall motion[11] and to study developing engineered tissues. [12] Magnetomotive OCE (MMOCE)[13] is a recent extension to magnetomotive OCT (MMOCT), [14] a novel technique that uses magnetic nanoparticles (MNPs) as contrast agents that are dynamically controlled by an external computer controlled electromagnet. MMOCE performs non-contact elasticity measurements using the embedded MNPs as internalized force transducers in real time. Chirped MMOCE is performed by externally manipulating the embedded MNPs using a temporally chirped magnetic field (0 to 1000 Hz). Quasi-static MMOCE, introduced in this paper, is performed by introducing a linearly stepped magnetic force on the embedded MNPs.

In this paper, we present the study of an *in vitro* model using MMOCE and demonstrate the feasibility of assessing mechanisms resulting in bronchiectasis. The *in vitro* model used consisted of human tracheo-bronchial-epithelial (hBE) cells grown on porous support at an air-liquid interface. The porous support is made of MNPs loaded into electrospun polyurethane and collagen to simulate the epithelium and sub-epithelial extracellular matrix. On these artificial membranes, hBE cells differentiate into an epithelium and exhibit coordinated cilia movement consistent with *in vivo* behavior. Using these *in vitro* membranes, we demonstrate that quasi-static MMOCE can track the elastic properties of the electrospun scaffolds, and that OCT can visualize the epithelial cell cultures similar to histology but non-destructively. We also investigate the morphology of *ex vivo* CF and normal lung airways using OCT and correlate the finding with histology. Finally, we present a quantitative study of elasticity in *ex vivo* normal and CF airways using chirped MMOCE.

2. METHODS

Our SDOCT system consists of an integrated pump and a Ti:Sapphire femtosecond laser (Griffin, KMLabs, Inc.). It produces an 800 nm beam with a bandwidth of 130 nm, corresponding to a coherence length of ~2.5 µm in air. The broadband light is launched into a single-mode fiber and directed into a free-space interferometer, which is divided into a sample arm and a stationary retroreflector in the reference arm (Fig. 1). The sample beam is steered using galvanometer controlled x-y mirrors placed one focal length above a 40 mm achromatic imaging lens (providing a transverse resolution of ~16 μm). The interference of the reference and the sample beams is measured with a spectrometer composed of a grating, imaging lens, and line camera (Piranha, Dalsa Inc.) operated at up to 20 kHz, providing an imaging depth of 2 mm in air.

Figure 1. MMOCE system. FSC: Free Space Collimator, BS: Beam Splitter, NDF: Neutral Density Filter, M: Mirror, R: Retro-reflector, FC: Fiber Coupler

2. 1. Lung tissue acquisition

CF and normal lungs were obtained under protocols approved by the University of North Carolina, School of Medicine Committee on the Protection of the Rights of Human Subjects. The CF lungs were explanted at the time of lung transplantation and the normal lungs were from organ donors whose lungs were deemed unsuitable for transplantation due to a variety of causes including age, smoking, acute lung injury/infection or lack of a suitable local recipient.

2.2. Artificial *in vitro* membrane fabrication

 The polyurethane scaffolds were fabricated by electrospinning a non-woven, porous membrane from a polymer solution of Pellethane® 2103-80AE (Dow Corning) and 30nm iron oxide (Fe_3O_4) nanoparticles (Sigma Aldrich) suspended in Dimethyl Formamide (DMF) and Tetra Hydrofuran (THF). The polymer solution was first sonicated for 30 minutes to reduce MNPs aggregation. The final polymer solution, 10% Pellethane and 4% iron nanoparticles by weight in a 1:1 THF:DMF solution, was electrospun for 90 minutes onto a collector plate. The Pellethane membrane were then cut into discs with diameters of approximately 1.1 cm and mounted onto containers as described in detail previously.[15] Each scaffold was then treated with a stock solution of Human Placental Collagen Type IV (Sigma C-7521). The collagen was allowed to dry overnight and then the scaffolds were sterilized with UV light for 30 minutes. Scaffold used in cell experiments was then seeded with 190,000 16-hBE cells suspended in DMEM/F12 media with 10% Fetal Bovine Serum. The hBEs seeded scaffold was left in the incubator for 7 hours to allow confluence between the 16-hBE and the artificial membrane. Control scaffold was also hydrated in DMEM/F12 media and placed in the incubator during this time so as to maintain similar conditions between the two scaffolds. The membranes were hydrated in DMEM/F12 throughout the study since the beginning the of the 7 hour incubation period and were kept in the incubator in between measurements.

2.3. Magnetomotive OCT

The MNPs embedded in the imaging volume to be imaged provide the basis for magnetomotive measurements. These dynamically controllable particles due to their small size can be accurately described as superparamagnetic and as a consequence, they dominantly experience translational forces when exposed to a magnetic field. The force experienced by a single MNP embedded in the membrane is given by:[16]

$$\vec{F}_{mag} = V(\chi_p - \chi_{med})\frac{\nabla|\vec{B}|^2}{2\mu_0} \tag{1}$$

where V is the imaging volume, and χ_p and χ_{med} are the magnetic susceptibilities of the MNPs and the surrounding medium respectively. This relation holds true as long as the magnetic field is sufficiently low such that the magnetization of the MNPs is linear (well below saturation magnetization). In our experiments, the magnetic fields are chosen to be sufficiently low such that this assumption is valid. The magnetic field gradient produced by the computer controlled solenoid magnet is directly proportional to solenoid control voltage, $V_{solenoid}$ i.e.

$$\nabla\vec{B} \propto V_{solenoid} \tag{2}$$

Thus, from equation (1) and (2), we see that as long as the magnetization of the MNPs doesn't attain saturation, the magnetic force applied to the MNPs and the surrounding membrane is proportional to the square of solenoid control voltage, i.e.,

$$\vec{F}_{mag} \propto V_{solenoid}^2 \tag{3}$$

Thus, for magnetomotive imaging, the magnetic force on the MNPs and the surrounding media is controlled indirectly by the computer controlled solenoid electromagnet that is synchronized with data acquisition and x-galvo mirror scanning (Fig. 1). The water-jacketed solenoid electromagnet is placed underneath the imaging lens and immediately above the sample for imaging. The central bore in the electromagnet allows the passage of the OCT imaging beam and the magnetic field gradient in the sample is dominantly in the axial direction and negligible in the radial direction. A programmable 250 W power supply is used to apply a magnetic field of ~0.15 T and a gradient of ~20 T/m within the sample imaging volume.

MMOCT was performed by modulating the magnetic field at 100 Hz while sampling at the camera scan rate of 1000 Hz. 2500 axial lines were chosen for each B-mode scan. The *in vitro* scaffolds were probed with 5.50 mW of optical power and the lateral scan was performed over a distance of 2 mm across the membrane. The power of the optical beam probing the airway samples was 14 mW and the lateral scan was performed over a distance of 1 mm. The airways were soaked overnight in Lactated Ringer's solution containing 20nm MNPs (Sigma Aldrich) at the concentration of 1mg/ml prior to performing MMOCT.

2.4. Magnetomotive OCE

To perform MMOCE, MNPs embedded in the sample are externally manipulated by a time-varying magnetic field and the resultant optical phase oscillations linearly proportional to the displacements of MNPs and the surrounding tissues are measured quantitatively.[17] Using magnetic nanoparticles as internalized force transducers circumvents contact problems inherent to external force transducers typically used in elastography.[18] Phase-sensitive spectral domain OCT (SDOCT) is employed to sense the nanometer-scale tissue deformations arising from magnetically manipulating the embedded MNPs.[19] We discuss two different MMOCE methods used in this paper below:

2.4.1. Quasi-static MMOCE on *in vitro* membranes

For the *in vitro* study using artificial membranes, a magnetic field gradient (2 Hz) is applied in increasing steps as shown by equation (4) to sequentially induce a linearly stepped force on the embedded MNPs. The solenoid electromagnet control voltage for the quasi-static measurement is stepped in the following manner:

$$V_{solenoid}(i) = V_{\max}\sqrt{\frac{i}{n-1}} \tag{4}$$

where $V_{\max}$ is the maximum voltage, n is the number of steps and i is the step and ranges from 0 to n-1.
From equation (3) and (4), we get:

$$F_{mag}(i) = V_{\max}^2\left(\frac{i}{n-1}\right) \tag{5}$$

It is clear from equation (5) that the magnetic force experienced by the embedded MNPs and the surrounding medium is linearly stepped. A representative linearly stepped magnetic force and the resultant displacement of the MNPs and the surrounding membrane are shown in Fig. 2. Under this linearly stepped magnetic force, spectral domain OCT data is acquired in M-mode to measure the time evolution of optical phase over a fixed axial line in the sample. Subsequently the resulting displacement Δz is deduced from the unwrapped phase φ in M-mode OCT based on the following equation:[20]

$$\Delta z(t) = \frac{\lambda}{4\pi n}\Delta\phi(t) = \frac{\lambda}{4\pi n}\big(\phi(t) - \phi(0)\big) \tag{6}$$

where n is the refractive index of the medium, t is time and λ is the central wavelength of the probing light and the phase shift $\Delta\varphi$ is computed by referencing the phase against its value at the beginning of the scan.

Since the solenoid control voltage squared is directly proportional to the magnetic force (equation (3)) and the resultant displacement can be indirectly extracted from unwrapped phase shift (equation (6)), we can get a qualitative measure of stiffness as follows:

$$Stiffness \equiv \frac{Applied\ Force}{Area \times Displacement} \propto \frac{V_{solenoid}^2}{\Delta z} \tag{7}$$

Thus, solenoid control voltage squared per unit displacement is a representative measure of stiffness, which is the measure of resistance offered by the sample in response to applied forces. In this way, the quasi-static force to displacement relationship can be deduced to determine the stiffness of the membrane.

Electrospun scaffolds were prepared, hydrated in DMEM/F12 solution and both control and hBE seeded scaffolds were placed in the incubator for 7 hours as described earlier in this paper. Subsequently, quasi-static MMOCE was performed at intervals of ~8 ½ hours for the next ~25 ½ hours. The OCT beam was focused at the center of the electrospun scaffolds with 5.50 mW of optical power from Ti:Sapphire femtosecond laser (Griffin, KMLabs, Inc.) centered at 800 nm and with a bandwidth of about 130 nm. The axial scans were performed at the camera scan rate of 1000 Hz and 2500 axial lines were chosen in a frame allowing a frame time of 2.5 seconds. The magnetic force was stepped from 0 to its maximum value in 5 discrete steps so each step consisted of 500 axial lines. Choosing a large number of axial lines per step allowed the system to reach mechanical equilibrium between each step. Micron-scale displacements between the steps and nanometer-scale displacements within each step were observed in response to the magnetic force (Fig. 2). The

displacement Δz was computed according to equation (6) by averaging the phase change at all axial positions with an OCT signal amplitude above a threshold value. The phase sensitivity was calculated as the standard deviation of the phase from a stationary mirror in the sample arm and was found to be 0.27 radians. Using the refractive index of the sample as 1.4, the central wavelength as 800 nm, the displacement sensitivity was calculated from unwrapped phase (equation (6)) to be 12.5 nm. Typical displacements measured in the samples are on the order of a few hundred nanometers.

Figure 2. (Bottom) Linearly stepped magnetic force in quasi-static MMOCE; magnetic force on the MNPs is directly proportional to the coil voltage squared according to equation (3). (Top) Displacement in response to the stepped magnetic force; blue curve is the actual displacement and the red curve is the mean displacement during each step with the error bar indicating the standard deviation of displacements within each step (0.5 seconds=500 axial lines).

2.4.2. Chirped MMOCE on lung airways:

In chirped-MMOCE, MNPs embedded in the sample are externally manipulated by a temporally chirped magnetic field (0 to 1000Hz) and the resultant time-dependent oscillations of the MNPs and the surrounding tissues are measured quantitatively. Similar to quasi-static MMOCE, the resulting displacements of the MNPs and the membrane are obtained from the optical phase changes using phase-sensitive SDOCT. The advantage over quasi-static MMOCE is that an absolute measure of the force is not needed to compute the elastic modulus, because longitudinal compression modes are observed as resonant mechanical frequencies and are directly relatable to the elasticity. The disadvantage of chirped MMOCE is that the samples must be nearly cylindrical with unbound sides for the longitudinal modes to be accurately modeled, which makes this technique inappropriate for studying the *in vitro* membranes.

To perform chirped-MMOCE on lung airway samples, a frequency-swept magnetic field gradient (0 to 1000 Hz) was applied to induce a chirped modulated force on the embedded MNPs. Due to the applied chirped magnetic field, the mechanical phase lag between the driving force and the displacement makes a transition from 0 to π at resonance (Fig. 9), a characteristic behavior of damped linear harmonic oscillators at resonance. This longitudinal resonant frequency can be directly related to the elastic modulus of the sample by following an inversion technique called magnetomotive resonant acoustic spectroscopy (MRAS), [21] which is analogous to resonant ultrasound spectroscopy.[22] In this technique, the tissue samples are modeled as vertical cylinders that have a closed boundary at the bottom (due to their weight) and open boundaries elsewhere. For longitudinal modes in the cylinder, the resonant frequency is directly proportional to the square root of the elastic modulus, E. The MRAS technique then finds the value of E that predicts the measured resonant frequency, as described in detail previously.[21] Since the MRAS model assumes the shape of the tissue to be cylindrical, the evaluated elastic modulus aren't exact. As a result of this simplification, the uncertainty in the exact dimensions of the sample is thus used to estimate the standard deviation of the fitted elastic modulus.

3. RESULTS AND DISCUSSION

3.1. Study of *in vitro* membranes using quasi-static MMOCE

An SEM image of an electrospun polyurethane scaffold used to grow the hBE cells is shown (Fig. 3A). hBE cells on these scaffolds grew well and differentiated normally as shown in the histological image (Fig. 3B). B-mode OCT image of a differentiated scaffold (Fig. 3C) suggests the presence of two cell layers, in accordance with histology. While we did not employ Doppler-mode OCT to look for cilia movement in this experiment, it may be possible to visualize the mucus layer and beating cilia using Doppler-mode OCT.

A representative plot of displacement in response to the stepped squared coil-voltage for control and hBE seeded scaffold at time intervals of ~8 ½ hours after the initial 7 hours of incubation time, is shown in Fig. 4. The slope of the lines in nm/V^2 is inversely proportional to stiffness according to equation (7). Thus, by tracking the slopes of the lines, we can track the relative change in stiffness of the membranes as a function of time.

Since the area of the membrane is constant, a quantitative measure of stiffness in terms of V^2/nm, according to equation (7) was evaluated for the data of Fig. 4 for comparative analysis at different times (Fig. 5). Note that, since the control membrane and the hBE seeded membrane were extracted from different locations of the electrospun membrane, the concentrations of MNPs in the two membranes are different due to which the actual force imparted by the magnet is different on the two membranes even though the same control voltage is used. This may explain the apparent mismatch in stiffness (in terms of V^2/nm) between the two samples at the beginning of the experiment. Thus, the reported stiffness values in V^2/nm should be considered for comparative study at different time scales for the same sample only.
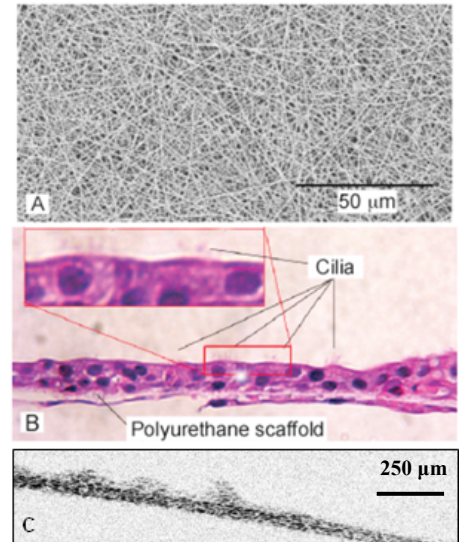

Figure 3. Electrospun scaffold, histology and OCT images of hBE cells. A) Polyurethane scaffold viewed by scanning electron microscopy (SEM). B) Histology of hBE cells grown on a polyurethane scaffold using Hematoxylin and Eosin (H&E) stains. C) B-mode OCT image (1.64 mm × 0.33 mm) of hBE cells on a polyurethane scaffold.
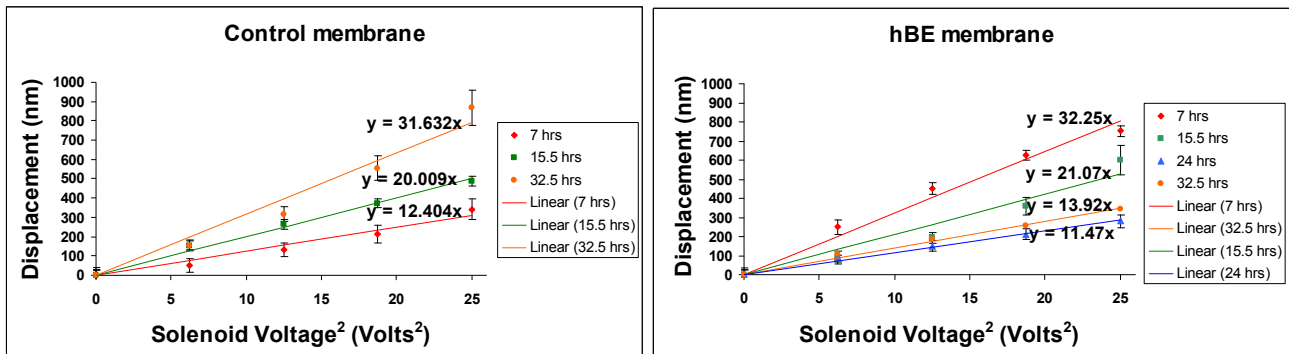

Figure 4. A representative displacement vs. squared solenoid-voltage plot for the control and hBE seeded membranes at ~8 ½ hour intervals. The slope of the lines in nm/V^2 is inversely proportional to stiffness according to equation (7). Each data point is the average displacement during each applied solenoid voltage and the uncertainty is estimated from a combination of standard deviation of displacement during the force step and the systematic uncertainty obtained with the magnetic field off.

As can be seen from Figs. 4 and 5, the control sample became less stiff as time elapsed. This is expected because, the control sample was hydrated in DMEM/F12 media and it is natural for the membrane to become softer the longer it is wetted. On the other hand, the hBE seeded membrane depicted an increased stiffness as time elapsed. It is surmised that as the hBE cells multiplied, they bonded tightly with the artificial membrane giving rise to an added tension in the

membrane that then portrayed as an increased stiffness of the composite membrane. The hBE coated membrane was also hydrated in DMEM/F12 media to sustain cell growth and it appears that the bonding effect of hBE cells and the scaffold more than offset the softening effect observed for the control scaffold.
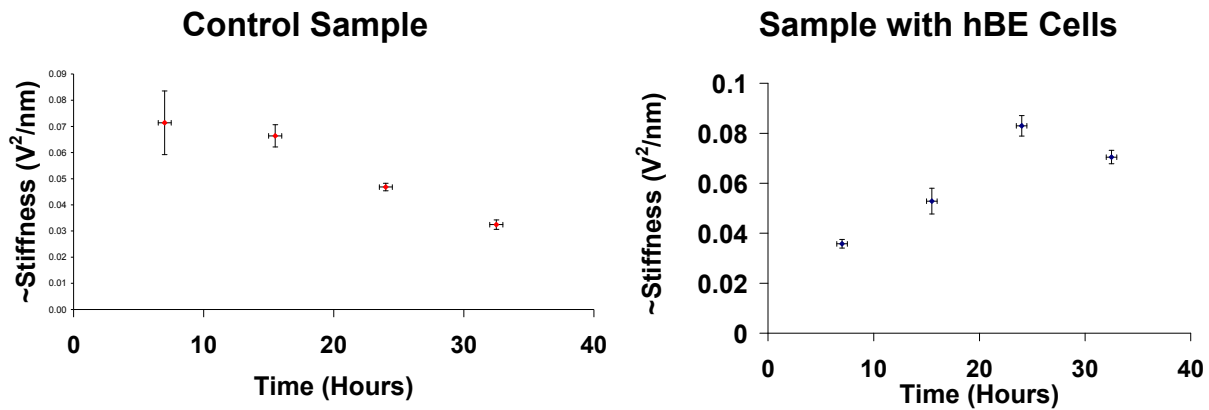

Figure 5. A relative stiffness measurement in terms of V^2/nm for the control and hBE seeded scaffolds. The first data point is at the end of the allowed confluence time of 7 hours for the hBE seeded scaffolds. Each of the data points thereafter are 8 ½ hours apart.

MMOCT was also performed on the scaffolds at the beginning and at the conclusion of the stiffness-tracking study (Fig. 6). The uniformity of magnetic signal at both times shows that the MNPs didn't seep out of the membrane into the hydrating media on which the membranes were kept. This suggests that the MNPs seeded artificial scaffolds are suitable for long term *in vitro* study using MMOCE. This along with the stiffness-tracking study suggests that MMOCE done on *in vitro* membranes is well positioned to analyze ECM remodeling in response to bacterial exposure by providing non-invasive assessment of the scaffold elasticity.
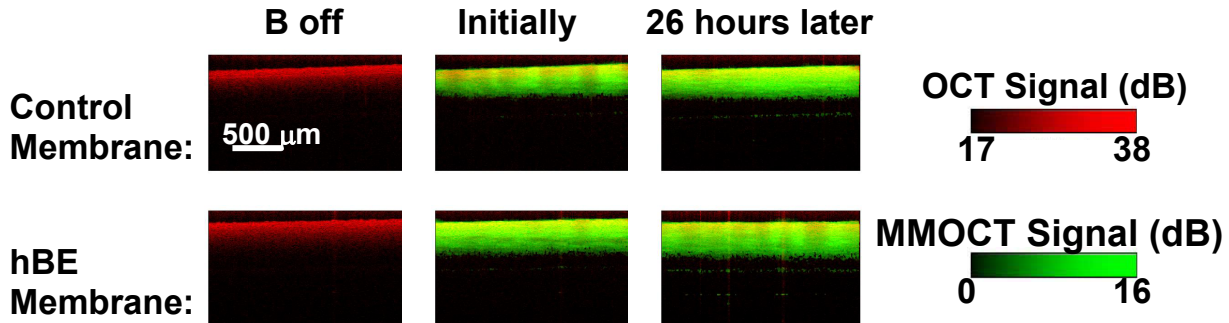

Figure 6. B-mode MMOCT images of control membrane (top) and hBE seeded membrane (bottom) at the start and the end of the experimental process. Red and green display the structural and magnetomotive image channels respectively, as indicated by the colored scale bars.

3.2. Correlative study of normal and CF airways

B-mode OCT images of CF and normal lung airways were acquired in this study (Fig. 7). The B-mode OCT image of a CF bronchiole shows a corrugated appearance of the inner wall, which is a characteristic structural feature of bronchiectasis (Fig. 7A). A smoother non-corrugated appearance is observed in the inner walls of a normal airway (Fig. 7C). Comparison of these morphological features with histology also confirms these findings. The excellent visualization of lung morphology afforded by OCT is promising and, coupled with elastography imaging, may eventually provide new clinical tools for monitoring bronchiectasis and correlating structure and function.
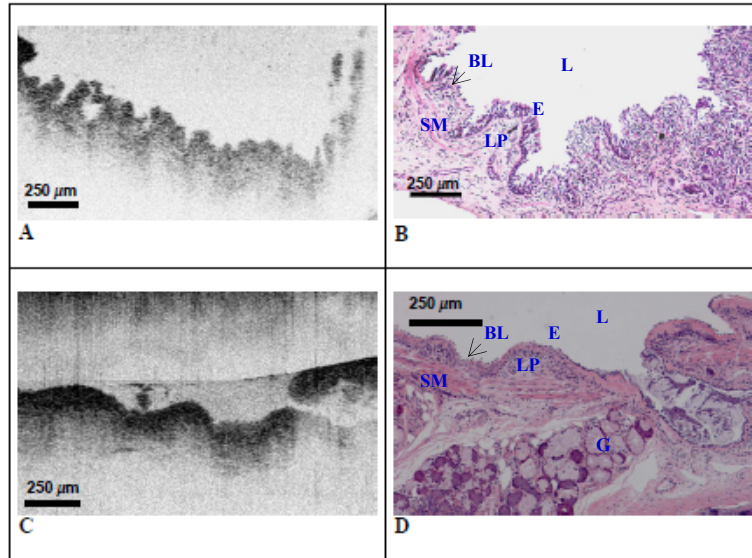
Figure 7. B-mode OCT slices (length × height). **A.** CF lung bronchiole showing corrugated inner walls; the airway lumen is above. **B.** Corresponding histology of the CF bronchiole using Hematoxylin and Eosin (H&E) stains **C.** Normal lung airway with a smoother appearance; the airway lumen is above. **D.** Corresponding histology of the normal bronchiole using H&E stains. Note: the exposure times are different for the two OCT images (100 µs for CF and 190 µs for normal).

L: Lumen
BL: Basal Lamina
E: Epithelium
LP: Lamina Propria
SM: Smooth Muscle
G: Gland

3.3. Elasticity of normal and CF airways using Chirped-MMOCE

To obtain a quantitative measure of the airway elasticity, MMOCE was performed on normal and CF lung airways that were soaked in Lactated Ringer's solution containing MNPs overnight. The MNPs diffused well into the airways as indicated by the magnetic signal produced by the MNPs in the MMOCT images (Fig. 8).

MMOCE was performed at the center of a normal airway sample (size: ~10 mm diameter) by sweeping the frequency from 0 to 1000 Hz while sampling at a camera line rate of 5000 Hz. From the observed resonant frequency (Fig. 9), the elastic modulus was extracted using the MRAS inversion technique and was found to be 8000 ± 3000 Pa.
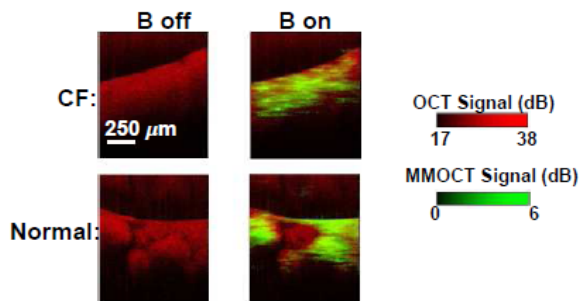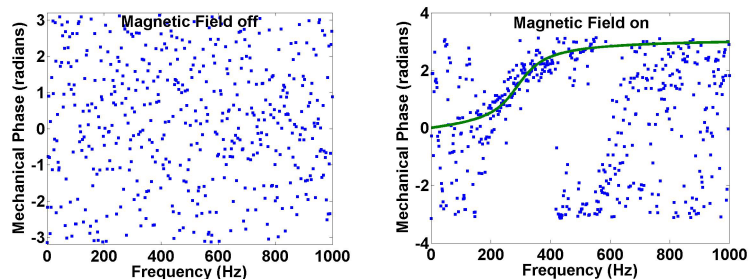

Figure 8. B-mode MMOCT image of CF airway (top) and normal airway (bottom) with the magnetic field off (left column) or modulated (right column). Red and green display the structural and magnetomotive image channels respectively, as indicated by the colored scale bars. MMOCE is performed at the center of the each sample.

Figure 9. MMOCE performed in a normal lung airway (~10mm in diameter). The resonant frequency is extracted using the fitted solid green line. Mechanical phase lag with the chirped magnetic force off (left) and on (right); a phase shift of π is observed at the resonant frequency when the chirped magnetic field is on. Extracted elastic modulus, $E = 8000 \pm 3000$ Pa.
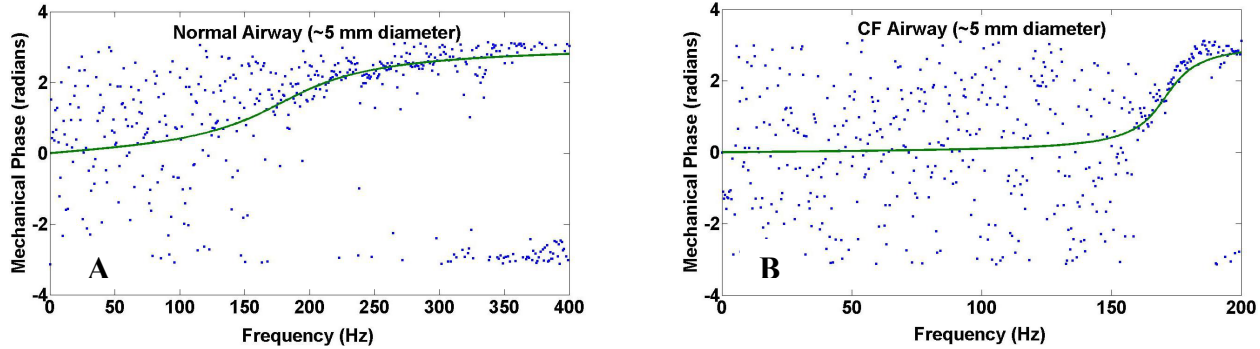
Figure 10. MMOCE in lung airway showing mechanical phase as a function of chirped magnet frequency. The resonant frequency is extracted using the fitted solid green line. **A.** Normal Lung airway (~5 mm in diameter); Extracted elastic modulus: 8000 ± 3000 Pa. **B.** CF Lung airway (~5 mm in diameter); Extracted elastic modulus: 3000 ± 1000 Pa.

MMOCE was also performed at the center of a smaller normal airway sample (size: ~5 mm diameter) by modulating the frequency from 0 to 400 Hz at a camera line rate of 2000 Hz (Fig. 10 A). A phase swing is observed across the resonant frequency and using the MRAS inversion technique, the elastic modulus was found to be 8000 ± 3000 Pa. MMOCE on a CF airway (size: ~5 mm diameter) was carried out by modulating the frequency from 0 to 200 Hz at a camera line rate of 1000 Hz (Fig. 10 B). From the resonant frequency, the elastic modulus was extracted using MRAS technique and was found to be 3000 ± 1000 Pa.

Table 1. Experimentally measured elastic modulus values of normal and CF lung airways:

Normal Airway (~10 mm diameter)	Normal Airway (~5 mm diameter)	CF Airway (~5 mm diameter)
E = 8000± 3000 Pa	8000 ± 3000 Pa	3000 ± 1000 Pa

The experimental elastic modulus values (Table 1) show an agreement between the two normal airway measurements. The elastic modulus of CF airway and normal airways are separated by greater than their uncertainties, suggesting a significant difference in their elastic moduli. This serves to corroborate the fact that the stiffness of airway walls in CF lung is reduced due to the breakdown of ECM in bronchiectasis. This demonstrates the feasibility of MMOCE to differentiate a normal airway from a bronchiectatic CF airway based on their elastic moduli. Various CF airways demonstrate varying degrees of degenerations depending on the airway size, patient's age and the severity of infection and inflammation. In this study, the airway elasticity measurements were carried out on finite samples and in the MRAS technique, the airway samples were assumed to have a cylindrical geometry, so discretion must be exercised in drawing definitive conclusions about the airways and their elastic moduli. Nevertheless, we have demonstrated that MMOCE is suitable for studying normal and CF airways and coupled with the *in vitro* study on membranes to non-invasively monitor elasticity changes arising from putative bronchiectatic mechanisms, it may become a diagnostic tool to assess the severity and the stage of the disease.

CONCLUSION

Lung disease is the most common cause of morbidity and mortality in CF patients. The cause of bronchiectasis, the predominant structural pathological change in lung tissue, is poorly understood. Using hBE cells grown on "home-spun" scaffolds as an *in vitro* model of the airway wall in combination with the novel MMOCE technique provides a powerful platform for studying mechanisms resulting in bronchiectasis. The morphological study of *ex vivo* CF and non-CF lung tissues with OCT and MMOCE may lead to new *in vivo* imaging and elastography methods to monitor disease progression and treatment. A greater understanding of basic pathogenic mechanisms in CF lung afforded by our novel *in vitro* technique may result in further advances in disease detection, monitoring and therapy in the future.[23]

REFERENCES

[1] McCormick,J., *et al.,* "Demographics of the UK cystic fibrosis population: implications for neonatal screening," *Eur. J. Hum. Genet.,* **10**, 583-590 (2002).

[2] Boucher R.C., "Molecular Insights into the Physiology of the 'Thin Film' of Airway Surface Liquid," *J. Physiol.,* **516**, 631-638 (1999).

[3] Morrissey B.M., "Pathogenesis of Bronchiectasis," *Clin Chest Med.,* **28**, 289-296 (2007).

[4] Huang D., *et al.,* "Optical Coherence Tomography," *Science,* **254**, 1178-1181 (1991).

[5] Fujimoto J.G., *et al.,* "Optical biopsy and imaging using optical coherence tomography," *Nature Med.,* **1**, 970–972 (1995).

[6] Schmitt J.M., "OCT elastography: Imaging microscopic deformation and strain of tissue," *Opt. Express,* **3**, 199-211 (1998).

[7] Ophir j., *et al.,* "Elastography: imaging the elastic properties of soft tissues with ultrasound," *J. Med. Ultrason.,* **29**, 155-171 (2002).

[8] Manduca A., *et al.,.* "Magnetic resonance elastography: *in vivo* non-invasive mapping of tissue elasticity," *Med. Image Anal.,* **5**, 237-254 (2001).

[9] Wilson L.S., *et al.,* "Elastography – the movement begins,' *Phys. Med. Biol.,* **45**, 1409-1421 (2000).

[10] Xing L., *et al,* " Modeling and measurement of tissue elastic moduli using Optical Coherence Elastography," *Proc. SPIE,* **6848**, 685803-8 (2008).

[11] Chan R.C., *et al.*, "OCT-based arterial elastography: robust estimation exploiting tissue biomechanics," *Opt. Express,* **12,** 4558-4572 (2004).

[12] Ko H.J., *et al.,* "Optical coherence elastography of engineered and developing tissue," *Tissue Eng.,* **12**, 63-73 (2006).

[13] Crecea V., *et al.,* "Magnetomotive nanoparticles transducers for optical rheology of viscoelastic materials," *Opt. Express,* **17,** 23114-231122 (2009).

[14] Oldenburg A.L., *et al.,* "Magnetomotive contrast for in vivo optical coherence tomography," *Opt. Express*, **13**, 6597-6614 (2005).

[15] Fulcher M.L., Gabriel S, Burns K.A., Yankaskas J.R., Randell S.H., "Well-differentiated human airway epithelial cell cultures," *Methods Mol. Med.,* **107**, 183-206 (2005).

[16] Hafeli U., *et al.,* [Scientific and Clinical Appications of Magnetic Carriers], Plenum Press, 218-221 (1997).

[17] Oldenburg A.L., *et al.,* "Imaging magnetically labeled cells with magnetomotive optical coherence tomography," *Opt. Lett.,* **30**, 747-749 (2005).

[18] Ogi H., *et al,.* "Contactless mode-selective resonance ultrasound spectroscopy: Electromagnetic acoustic resonance," *J. Acousto. Soc. Am.,* **106**, 660-665 (1999).

[19] Oldenburg A.L., *et al.,* "Phase-resolved magnetomotive OCT for imaging nanomolar concentrations of magnetic nanoparticles in tissues," *Opt. Express,* **16,** 11525-39 (2008).

[20] Joo C., *et al.,* "Spectral-domain optical coherence phase microscopy for quantitative phase-contrast imaging," *Opt. Lett.,* **30**: 2131-2133 (2005).

[21] Oldenburg A. L. and Boppart S. A., "Resonant acoustic spectroscopy of soft tissues using embedded magnetomotive nanotransducers and optical coherence tomography," *Phys. Med. Biol.,* (submitted)

[22] Maynard J., "Resonant ultrasound spectroscopy," *Phys. Today,* **49**, 26-31 (1996).

[23] Dinwiddie R., "Pathogenesis of Lung Disease in Cystic Fibrosis," *Respiration,* **67**, 3-8 (2000).